Brodogradnja Volume 77 Number 1 (2026) 77104

University of Zagreb
Faculty of Mechanical
Engineering and Naval
Architecture

journal homepage: www.brodogradnja.fsb.hr

Brodogradnja

An International Journal of Naval Architecture and
Ocean Engineering for Research and Development

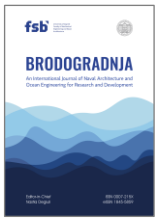

Performance enhancement of Savonius hydrokinetic turbines: the role of twisted blade profiles

Doğa Derman Çiçek, Elif Oğuz[*]

Department of Civil Engineering, Middle East Technical University, 06800, Ankara, Turkey

ARTICLE INFO

Keywords:
Savonius Hydrokinetic Turbine
Hydrokinetic Energy
Helical Blades
Blade Twist Angle
CFD

ABSTRACT

Savonius Hydrokinetic Turbines (SHTs) are widely recognized for their simplicity, cost-effectiveness, and adaptability to slow flow conditions. However, conventional SHT designs face limitations, including low efficiency and significant torque fluctuations. The adoption of twisted/helical blade profiles has emerged as a potential solution to enhance turbine performance by reducing torque fluctuations and improving power output. A review of the existing literature reveals that studies focusing on blade twist angles are limited. To address this, the present study systematically investigates the impact of a broader range of blade twist angles (15-90°) on SHT performance using computational fluid dynamics (CFD). Key performance metrics, including the torque coefficient (C_T) and power coefficient (C_P), were evaluated, and numerical accuracy was ensured through mesh independence and time step independence studies. The developed CFD model was validated against experimental results obtained from the literature to confirm the model's ability to capture flow dynamics. The results show that the SHT with a 45° blade twist achieves a maximum C_P of 0.252, an increase of 3.81 % over the conventional design, and reduces torque fluctuations by 9.38 %. Meanwhile, the 60° blade twist demonstrates comparable C_P values but achieves a further 7.28 % reduction in torque fluctuations compared to SHTs with a 45° blade twist.

1. Introduction

Global electricity consumption increased by 75 % between 2000 and 2018, with projections suggesting an additional 58 % rise by 2040 [1]. This shift underscores the importance of renewable energy resources, particularly hydrokinetic energy, which offers a predictable and abundantly available alternative [2-5]. Hydrokinetic energy is derived from the kinetic energy of water currents in rivers, canals, and tidal flows, providing a cleaner and less invasive option compared to traditional hydropower systems. The United States Department of Energy reports theoretical hydrokinetic potentials between 3620-4666 TWh annually, with 1285-1846 TWh being extractable, equivalent to 31.6-45.2 % of the nation's yearly energy production [6]. These figures emphasize the need for efficient hydrokinetic turbine technologies to harness this resource effectively.

[*] Corresponding author.
E-mail address: elifoguz@metu.edu.tr

https://doi.org/10.21278/brod77104
Received 21 April 2025; Received in revised form 28 August 2025; Accepted 28 August 2025
Available online 10 September 2025
ISSN 0007-215X; eISSN 1845-5859

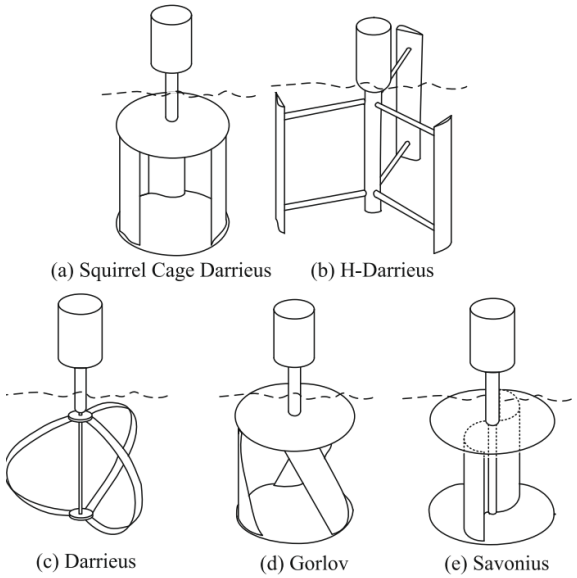

Fig. 1 Cross-flow turbine designs [7]

Among the various cross-flow hydrokinetic turbine types (Figure 1), Savonius Hydrokinetic Turbines (SHTs) stand out due to their simplicity, cost-effectiveness, and adaptability to low-velocity water flows [8-11]. As a drag-based design, SHTs harness energy through the difference in drag forces on their semi-circular blades, enabling effective operation in slow-moving or shallow waters [8-10, 12]. Despite these benefits, conventional SHT designs face inherent limitations, including low efficiency and significant torque fluctuations during power generation [8, 9, 11]. To overcome these challenges, researchers have investigated various optimization techniques, including modifications to blade profiles.

The integration of twisted blades in SHTs presents considerable potential for enhancing the power production capacity of SHTs. Twisted blades introduce a continuous phase difference along the turbine's height, reducing torque fluctuations in a manner similar to multi-stage SHTs. In this context, the twist angle refers to the angular displacement between the blade profile at the top and bottom of the rotor along the vertical axis. This geometric modification can contribute to improved efficiency and operational stability. A review of optimization studies on the implementation of twisted blades in SHTs is presented in the following.

Zullah et al. [13] conducted a numerical study to evaluate the performance of a SHT utilized in an oscillating water column (OWC) for wave energy conversion. The researchers tested three different models of the SHT, each with 3 blades and distinct twisted blade angles of 0°, 15°, and 30°. According to the results, the turbine having 30° twisted blades achieved the highest total efficiency of 12.64 %, 6.4 % higher than that of the turbine without twisted blades. Kumar and Saini [14] carried out a numerical study to evaluate the impact of applied blade twist angles of 0°, 12.5° and 25° on the performance of a two-semicircular-bladed SHTs with an aspect ratio (AR) of 1.58 and an overlap ratio (OR) of 0. The researchers tested these twist angles under varying inlet velocities ranging from 0.5-2 m/s to observe the effect of Reynold's Number (Re) on the model's performance. The findings of this study showed that the turbine with 12.5° twisted blades generated the highest C_p of 0.39 at 0.9 tip speed ratio (TSR) under 2 m/s flow velocity. Moreover, the increase in Re resulted in increased power generation for all studied twist angles. In a subsequent study, Kumar and Saini [15] investigated the effect of the blade arc angle and blade shape factor on the performance of the SHT with 12.5° twisted blades. The same test conditions utilized in the previous study were applied for the testing of the new configuration. The results showed that the SHT with a 150° arc angle and a shape factor of 0.6, combined with 12.5° twisted blades, generated a maximum C_p of 0.426, 9.23 % higher than that of its semicircular-bladed counterpart. Hadi et al. [16] conducted an experimental investigation to examine the effect of twisted blades on the performance of SHTs in a water pipe. The studied turbine had an AR of 1 and an 82 mm diameter without any overlap. Tests were conducted for 4 different discharges: 0.0029 m^3/s, 0.0057 m^3/s, 0.0081 m^3/s, and 0.0119 m^3/s. Blade twist angles of 0°, 12.5°, 30°, 45° and 60° were tested under these

conditions. According to the findings of the study, the turbine with 60° twisted blades showed superior performance at up to 0.0081 m^3/s discharge. However, the turbine without twisted blades exhibited higher performance at 0.0119 m^3/s discharge. Mosbahi et al. [17] carried out an extensive study incorporating both experimental and numerical investigations to examine the effect of a new deflector system on the performance of a three-bladed SHT. The researchers tested the performance of the three-bladed SHT with 30° twisted blades in an irrigation channel at/with under 0.86 m/s flow velocity. Then, the data obtained was used to validate the numerical model developed for the optimization of the proposed deflector system. The results showed that while the three-bladed SHT without the deflector system generated a C_p of 0.125 at TSR 0.7, the proposed deflector system increased the generated C_p by 12 %. In a separate publication, Mosbahi et al. [18] utilized the same 30° twisted blades for a two-bladed SHT configuration, tested under the same experimental conditions. Moreover, the same proposed deflector system was also re-optimized for the two-bladed version. The results highlight that the two-bladed configuration without a deflector system generated a C_p of 0.166 at a TSR of 0.78, 32.8 % higher than that of its three-bladed counterpart. Furthermore, the deflector system further increased the performance of the two-bladed SHT by 17.5 %. Patel et al. [19] conducted a numerical investigation to evaluate the performance of a SHT with 60° twisted blades across a wide range of TSR values at a flow velocity of under 0.924 m/s. Their results showed that the turbine achieved a maximum C_P of 0.2434 at a TSR of 0.884. Nag and Sarkar [20] conducted a comprehensive study integrating both experimental and numerical investigations to compare the performance of a conventional SHT, a modified SHT with an overlap and larger shaft diameter, and a helical SHT with a blade arc angle of 124° and a 90° blade twist angle. The rotor diameters and ARs of the turbines were kept constant. The experimental tests were carried out on a rectangular open channel with a 1 m/s freestream flow velocity. The researchers also placed a converging-diverging duct with a constant duct angle of 29° to observe its impact on the performance of the tested turbine variations. The result of the experimental study was used to validate the developed numerical model. Then, the numerical model was utilized to extend the studied freestream velocity to 2 m/s and 3 m/s and the studied duct angles to 20-32°. According to the findings, the helical SHT showed superior performance among the studied configurations, achieving a maximum power generation of 1.58 W at 1 m/s freestream velocity without a duct, 9.7 % higher than that of a conventional one. Moreover, the helical SHT with a duct generated 26 % and 48 % higher power than the conventional SHT with a duct and the conventional SHT without duct, respectively. Rengma et al. [21] conducted both numerical and experimental investigations to evaluate the effect of adopting twisted blades on the performance of a SHT. In the first phase, an experimental study was performed to assess the performance of a conventional SHT with straight semicircular blades at a flow velocity under 0.6 m/s, for TSR values ranging from 0.5 to 1.3. The results from this experiment were then used to validate a numerical model, which was subsequently utilized to analyze SHTs with twisted blade profiles. The study considered twist angles ranging from 0° to 180° and TSR values ranging from 0.6 to 1.1. The numerical results indicated that the SHT with 120° twisted blades exhibited the highest performance among the tested geometries, achieving a C_P of 0.19 at a TSR of 0.8, which represents a 6 % improvement over the conventional straight-blade design. Furthermore, by adopting a 120° twisted Bézier blade profile, the researchers reported an additional 14.7 % increase in performance compared to the standard 120° twisted blade.

Comparative studies focusing on the performance of SHTs with varying blade twist angles remain limited in the current literature. Among the studies on the adaptation of twisted blades in SHTs, only three [14, 16, 21] have specifically focused on comparing the effects of different blade twist angles, with two of them [14, 16] investigating a relatively narrow range. Rengma et al. [21], in contrast, examined a broader range (0-180°) and identified 120° as the most efficient configuration at $Re = 1.2\times10^5$.

On the other hand, three studies have extensively investigated the adaptation of twisted blade configurations in Savonius wind turbines (SWTs), considering a wide range of twist angles [22-24], along with other comparative studies focused on SWTs that examined a more limited set of twist angles [25-28]. Lee et al. [22] tested conventional SWTs with twist angles of 0°, 45°, 90°, 135°, and 180° at $Re = 8.4\times10^5$ and reported the highest power coefficient at 45°. Similarly, El-Askary et al. [23] tested modified Savonius blade sections with twist angles from 0° to 180° at $Re = 1.6\times10^5$ and observed peak performance at 45°. Saad et al [24] also investigated the performance of SWTs with twisted blade angles of 0°, 45°, 90°, 135°, and 180° at a $Re = 1.2\times10^5$ with overlap ratios (ORs) of 0.0 and 0.15. Similar to studies of Lee et al. [22] and El-

Askary et al. [23], the highest performance is obtained by the SWT with 45° twisted blades for both tested ORs. Notably, all three studies [22-24] reported a substantial drop in performance beyond a twist angle of 90°, with 120° and 135° yielding some of the lowest power coefficients. These findings contrast with those of Rengma et al. [21], who reported that 110°, 120°, and 130° twist angles produced the best performance among their tested cases, despite these angles showing poor results in the aforementioned SWT studies.

While studies on both SHTs [14, 16, 21] and SWTs [22-24] offer insights, they do not provide a unified understanding of twist angle effects, particularly when accounting for differences in working fluids and flow regimes [29, 30]. The conflicting findings between Rengma et al. [21] and SWT-focused studies further highlight the necessity for systematic investigation into the effects of twist angle in SHTs. Moreover, although multiple investigations on SWTs [14, 16, 21] have consistently identified the twist angle range of 30-90° as yielding optimal performance, this interval has not been comprehensively explored within the context of SHTs.

This study addresses these limitations by explicitly focusing on the 0-90° range, and systematically investigating twist angles of 0°, 15°, 30°, 45°, 60°, 75°, and 90° to assess their impact on SHT performance. By integrating flow visualization techniques, it aims to provide a deeper understanding of the influence twisted blade profiles have on SHT performance. This research not only bridges a critical gap in literature but also offers significant contributions to advancing SHT designs and optimizing their operational efficiency. Furthermore, the findings serve as a critical reference for future innovations, providing a foundation for the development of novel and more efficient turbine configurations, including advanced hybrid SHT designs tailored for diverse flow conditions.

The initial step of the investigation was to validate the developed CFD model by comparing its results with experimental results. The numerical model was then modified to account for the effects of different twist angles to investigate the impact of blade twist on SHT performance. The results then present the impact that different blade twist angles have on torque and power coefficients, and hence the flow characteristics around SHT, at various TSRs.

2. Methodology

This study investigates the effect of helical blade profiles on the performance of the studied SHT model using numerical methods.

SHTs, with semi-circular blades, extract energy from water currents using drag and viscous forces. Unlike streamlined propeller turbines, their asymmetric blade motion disrupts flow patterns and creates counter-flow streamlines influenced by the returning blade. Accurately resolving these viscous effects is critical for calculating net torque. Furthermore, experimental flow visualization methods such as PIV and PTV have revealed that the flow field around SHTs is inherently turbulent [31-35]. Building on these insights, this study employs CFD for transient simulations to capture complex flow phenomena such as flow separation, vortex shedding, and drag effects. These analyses provide a deeper understanding of the performance of helical blade profiles under turbulent conditions.

2.1 Governing Equations

2.1.1 Navier-Stokes Equations

The flow field in this study is governed by the Reynolds-Averaged Navier-Stokes (RANS) equations, where flow variables are decomposed into time-averaged and fluctuating components:

$$u_i = \bar{u}_i + u_i' \tag{1}$$

$$P = \bar{P} + P' \tag{2}$$

$$\frac{\partial \bar{u}_i}{\partial x_i} = 0 \tag{3}$$

$$\rho \frac{\partial \bar{u}_i}{\partial t} + \rho \bar{u}_j \frac{\partial \bar{u}_j}{\partial x_j} = -\frac{\partial \bar{P}}{\partial x_i} + \frac{\partial}{\partial x_j}\left[\mu\left(\frac{\partial \bar{u}_i}{x_j} + \frac{\partial \bar{u}_j}{\partial x_i}\right) - \rho\overline{u_\iota{}' u_j{}'}\right] \tag{4}$$

Here, ρ is fluid density, $\bar{u}$ is mean velocity, u' is the fluctuating velocity component, $\bar{P}$ is mean pressure, and μ is the dynamic viscosity. The term $-\rho\overline{u_\iota{}' u_j{}'}$ represents the Reynolds stress tensor, which introduces additional unknowns that require turbulence modeling for closure.

2.1.2 Turbulence Model

The complexity of turbulence requires the use of appropriate turbulence models for accurate CFD simulations of SHTs. Among the available models, the Shear Stress Transport (SST) *k-ω* turbulence model, developed by Menter [36, 37], has gained widespread acceptance for its robust predictive capabilities. This model combines the strengths of *k-ε* and *k-ω* formulations through a blending function that transitions between the two, enabling precise predictions in both the boundary layer and freestream regions.

Numerous studies have evaluated the performance of turbulence models for simulating SHTs. Dobrev and Massouh [31] compared the SST *k-ω* and Detached Eddy Simulation (DES)-SST *k-ω* models. While the DES-SST *k-ω* model demonstrated superior accuracy in matching experimental data, its computational cost was significantly higher. The 3D simulations using the SST *k-ω* model, however, provided good agreement with experimental results. Similarly, Nasef et al. [38] compared multiple turbulence models, including RNG *k-ε*, Realizable *k-ε*, and SST *k-ω*, and found the latter to be the most accurate for predicting C_T. Ferrari et al. [39] also reported that the SST *k-ω* model estimated the experimental results within a 12 % margin of error, while the Realizable *k-ε* and Spalart–Allmaras models produced deviations at around 20 %. In a 2D study, Alom et al. [40] compared multiple models and reported that the SST *k-ω* model resulted in the lowest deviation from experimental data (16.8 %), followed by the Transition SST model (20.0 %) and the RNG *k-ε* model (23.2 %). Based on its proven accuracy and reliability in previous studies, this research also adopts the SST *k-ω* turbulence model.

2.2 Performance Evaluation Parameters

The performance of the SHT is measured using the torque coefficient (C_T) and the power coefficient (C_P). The C_T indicates the proportion of torque generated by the turbine relative to the total torque available in the water flow across the turbine's projected area. It is expressed mathematically as:

$$C_T = \frac{T_{out}}{\frac{1}{2}\rho V_0^2 A_{ref} r} \tag{5}$$

Here, T_{out} represents the torque generated by the turbine, V_0 is the inflow velocity, ρ is the density of the fluid, A_{ref} is the turbine's projected area (calculated as the product of its height (H) and diameter (D)), and r refers to the turbine's radius.

The C_P measures the fraction of the available power in the water flow that is harnessed by the turbine. It is calculated as follows:

$$C_P = \frac{P_{ext}}{P_{av}} = \frac{T_{out}\,\omega}{\frac{1}{2}\rho V_0^3 A_{ref}} \tag{6}$$

In this equation, ω denotes the angular velocity of the turbine, P_{ext} is the power harnessed by the turbine, and P_{av} represents the total available power in the water flow. The numerator ($T_{out} \times \omega$) corresponds to the turbine's mechanical power, while the denominator ($\rho V_0^3 A_{ref}/2$) specifies the power in the water flow across the turbine's projected area.

To analyze turbine performance across various operating conditions, the torque and power coefficients are plotted against various TSRs. The TSR is defined as the ratio of the blade tip speed to the incoming flow velocity and is given by:

$$TSR = \frac{\omega R}{V_0} \tag{7}$$

These parameters are critical for evaluating turbine performance, providing insights into the operational range, and identifying conditions for maximum energy extraction.

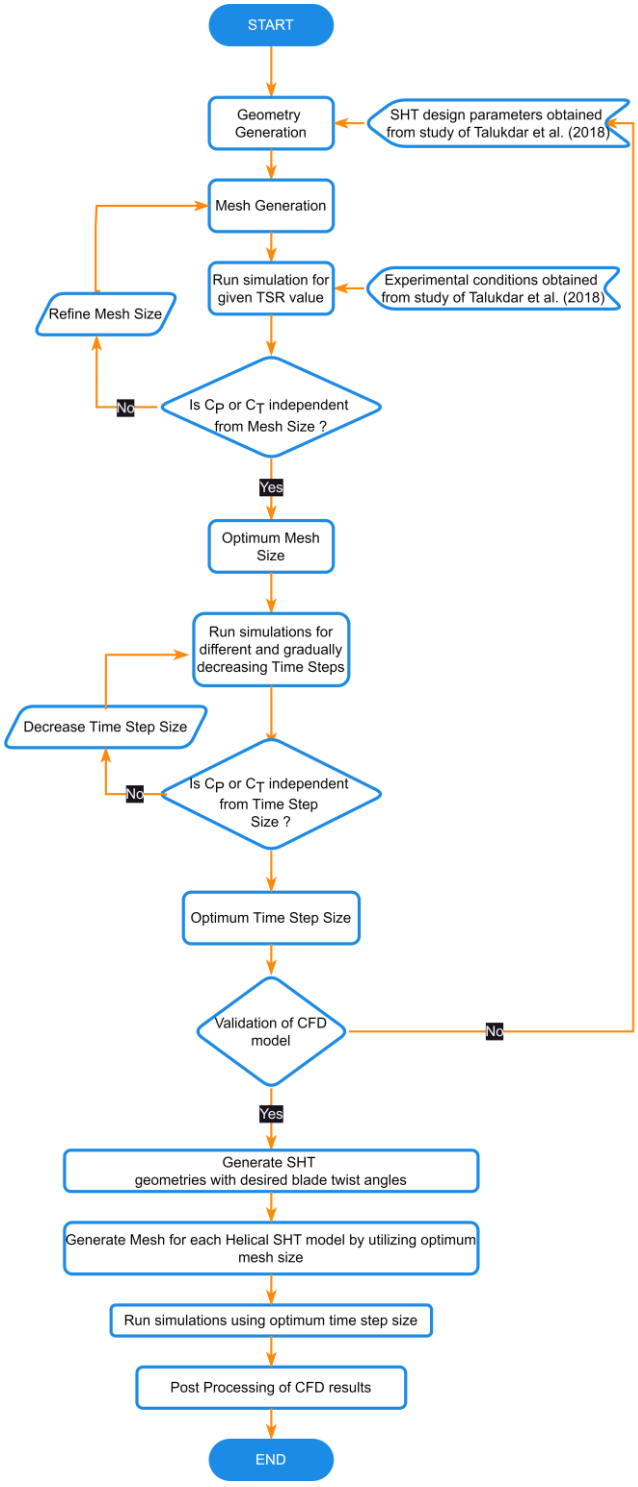

Fig. 2 Workflow for numerical modeling and validation, outlining steps from geometry generation to flow visualization and performance analysis

3. Numerical Modelling

This section outlines the methodology for developing and validating the CFD model designed to replicate real-world flow conditions accurately. The workflow, including validation and refinement processes, is presented in the flowchart illustrated in Figure 2.

3.1 Benchmark Case

The experimental study conducted by Talukdar et al. [41] was used as a benchmark case in this study. Their research focused on the impact of factors such as elliptical blade shapes, immersion levels, and blade count on the performance of SHTs.

3.1.1 Experimental Setup

As outlined by Talukdar et al. [41], the experiments were conducted in a flume located at IIT Guwahati's water treatment plant. The open channel measured 1 m in width and 0.9 m in height, with tests performed in its converging section, where the width narrowed to 0.58 m and the flow velocity was maintained at 0.8 m/s (Figure 3(a)(b)). The experimental setup included a vertically mounted SHT, and a support structure equipped with a pulley system connected to spring balances for torque measurement. During the tests used for validation in the present study, the turbine operated at a 100 % immersion level, meaning it was fully submerged below the free surface. Figure 3(c) illustrates the apparatus used in their experiments. The measurement precision for TSR and C_P was reported as ±1.5 % and ±2.12 %, respectively, reflecting the reliability of the experimental data [41].

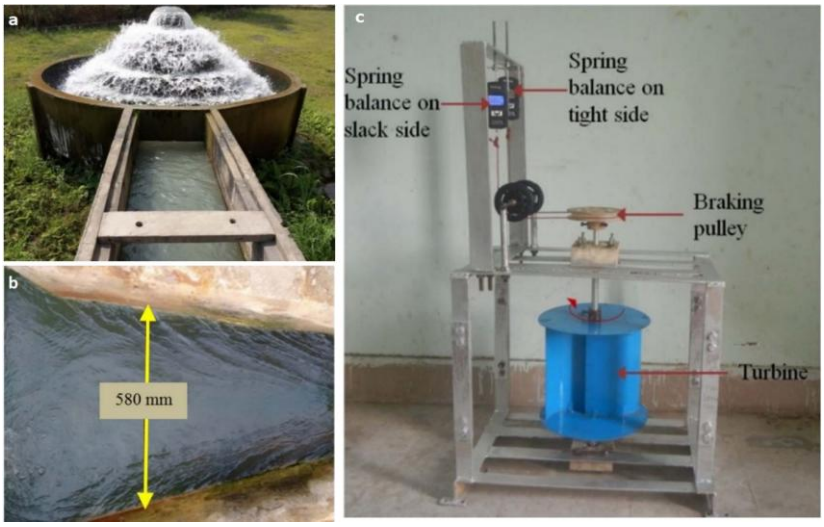

Fig. 3 Experimental flume setup: (a) the open channel with dimensions of 1 m width and 0.9 m height, and (b) the converging section (0.58 m width) where flow velocity was maintained at 0.8 m/s; (c) Overview of the experimental setup used to evaluate SHT performance [41]

3.1.2 Turbine Design and Geometry

Talukdar et al. [41] investigated a two-bladed Savonius Hydrokinetic Turbine (SHT) with a total height of 250 mm. The semicircular blades, 1.3 mm in thickness, were made from mild steel sheets and attached to a central shaft with a diameter of 16 mm. The turbine's design incorporates an OR of 0.15, resulting in an overall diameter of 250 mm. To improve stability, endplates with a diameter of 277.2 mm were fixed to the top and bottom, however, their thickness was not specified in the study of Talukdar et al. [41]. The turbine's geometric configuration is illustrated in Figure 4, and a detailed summary of its design parameters are provided in Table 1.

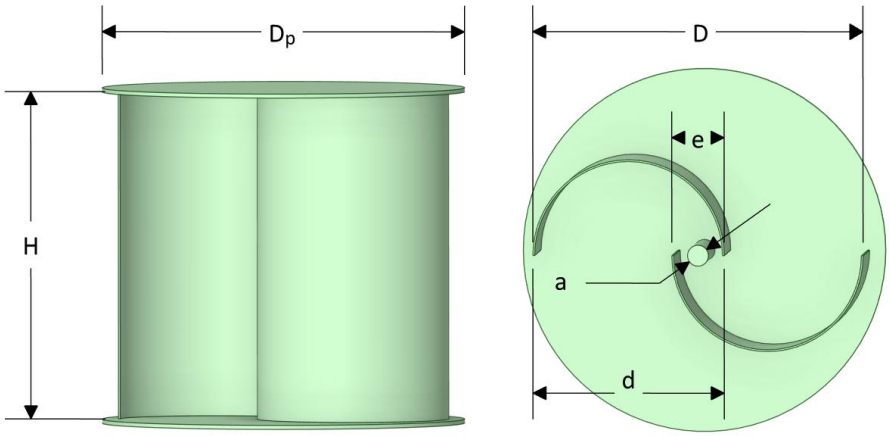

Fig. 4 Turbine design used by Talukdar et al. [41]

Table 1 Design parameters of the turbine used by Talukdar et al. [41]

Parameters	**Value**	**Unit**
Height of the turbine (*H*)	250	mm
Diameter of the turbine (*D*)	250	mm
Diameter of the blade (*d*)	144	mm
Diameter of central shaft (*a*)	16	mm
Endplate Diameter (D_{plate})	277.2	mm
Overlap Ratio (*e*/*D*)	0.15	-

3.2 Domain Configuration and Mesh Generation for SHT Analysis

Two computational domains were created to simulate the turbine's performance: a cylindrical Rotational Domain, representing the turbine and its rotation, and a rectangular prism Static Domain, representing the surrounding flow field. The Rotational Domain was designed to have a diameter of 1.5*D* and a height of 300 mm [42-47]. The turbine geometry, based on the parameters presented in Table 1, is positioned at the center of the domain. Figure 5 illustrates the Rotational Domain.

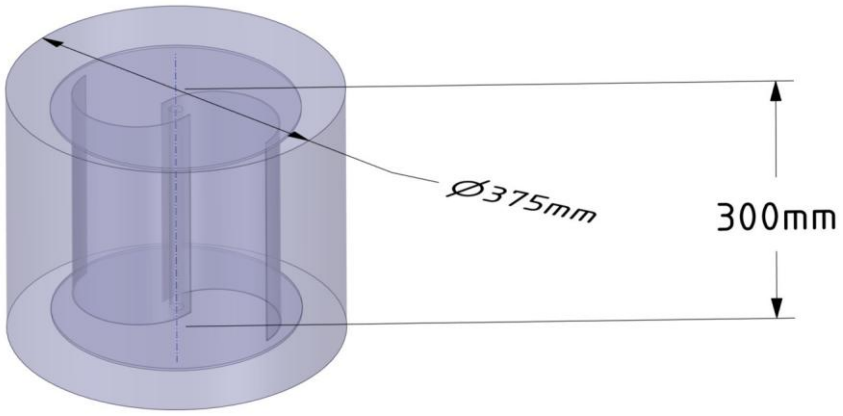

Fig. 5 Rotational Domain geometry for turbine simulations, illustrating the cylindrical domain housing the turbine

The Static Domain includes a cylindrical void at its center to house the Rotational Domain. The domain thickness is 580 mm, corresponding to approximately 2.3×*H***,** comparable to or larger than those used in similar studies reported in the literature [29, 43, 45, 48, 49]. The side boundaries are placed at 2.5*D* from the turbine, with the inlet and outlet positioned 3D and 5D from the turbine [29, 42, 43, 48], as shown in Figure 6.

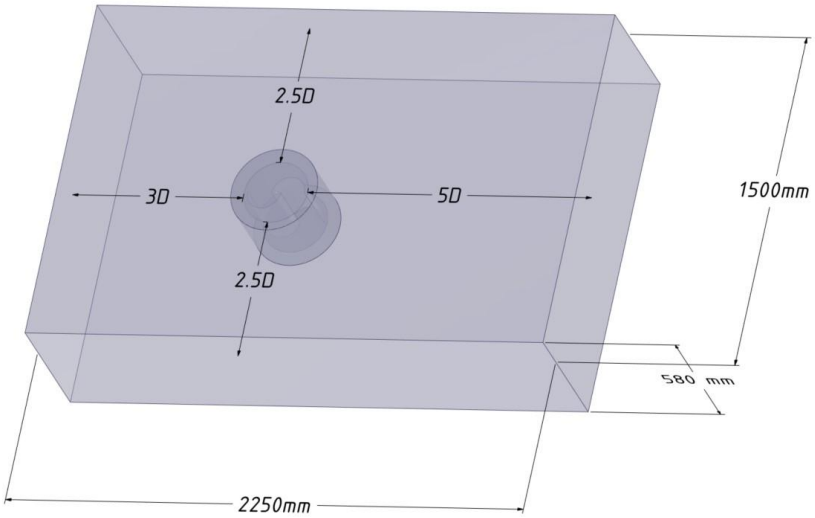

Fig. 6 Static Domain geometry for turbine simulations, showing the rectangular prism domain with a cylindrical void to house the Rotational Domain

The Rotational Domain is meshed using a combination of structured and unstructured elements to accommodate the complex curvature and thin profiles of the turbine blades. To accurately resolve the boundary layer, an inflation layer is applied, with $y^+ \approx 1$ [31, 38, 39, 48, 50, 51]. The resulting mesh for the Rotational Domain and the inflation layers around the SHT walls is illustrated in Figure 7.

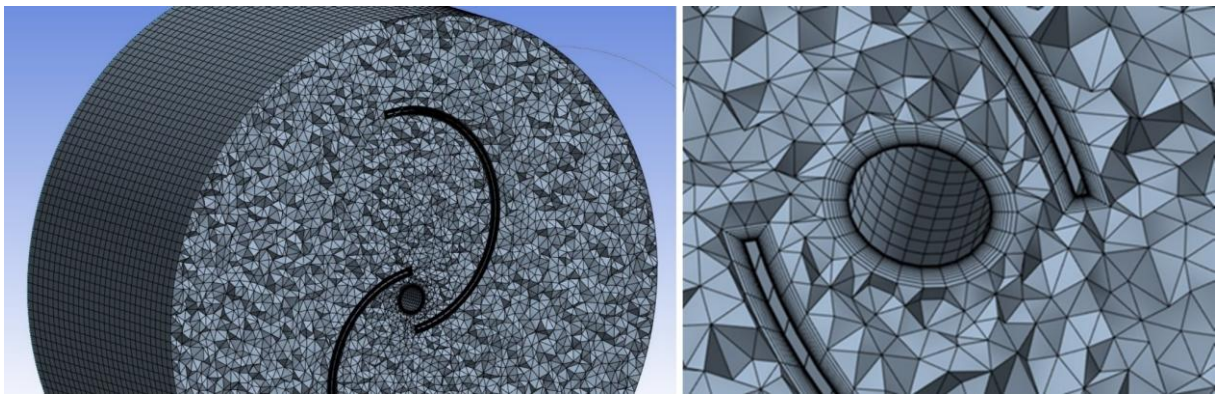

Fig. 7 Mesh configuration of the Rotational Domain

The Static Domain is meshed with unstructured tetrahedral elements. The mesh ensures smooth data transfer between the Static and Rotational Domains and provides sufficient resolution for accurate flow simulations. Figure 8 illustrates the generated mesh and its details near the Rotational Domain.

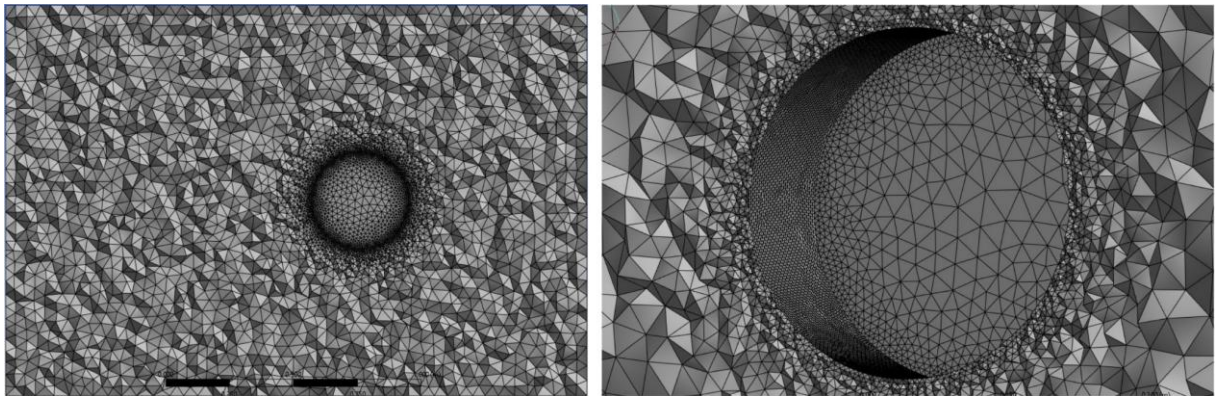

Fig. 8 Mesh of the Static Domain for modeling the external flow field around the turbine.

3.3 Numerical Approach for Simulating Rotating SHT Model

In this study, transient CFD simulations were performed to analyze the complex flow dynamics around the rotating SHT model used by [41]. These simulations advanced incrementally over discrete time steps, with initial conditions derived from steady-state simulations to ensure smoother convergence.

For steady-state simulations, the turbine's rotation was modeled using a moving reference frame, which modifies the RANS equations to account for the additional acceleration components induced by rotational motion. However, in transient simulations the turbine's rotation was represented using the sliding mesh model, which allows the actual rotation of the turbine blades to be directly simulated within the computational domain. Both steady-state and transient simulations were conducted using ANSYS Fluent.

A pressure-based solver with absolute velocity formulation was employed for both types of simulations. The Coupled Solver was preferred in both steady-state and transient simulations for its stability and faster convergence, despite requiring more memory than the SIMPLE Solver.

3.3.1 Mesh Independence Analysis for SHT Simulations

A mesh independence study was performed to identify the grid resolution beyond which further refinement no longer affects the simulation results. This study employed six different mesh configurations, each generated by progressively refining the grid, especially within the Rotational Domain and at the interface region.

Simulation parameters were kept constant across all mesh configurations, and simulations were carried out at a TSR of 0.6. To ensure accurate temporal resolution, a time step corresponding to 1 degree of turbine rotation (Δt=0.004545 s) was used [17, 18, 31]. Achieving $y^+ \approx 1$ was targeted for all meshes, but this resolution was unattainable in the inflation layers of the coarser grids (Mesh 1 and Mesh 2). The results are presented in Table 2, showing variations in the C_T and C_P across mesh levels.

Table 2 Mesh Independence Study: Obtained C_T and C_P values

Mesh No.	C_T	C_P	Discrepancy (%)
Mesh 1	0.356	0.214	-
Mesh 2	0.340	0.204	4.440
Mesh 3	0.346	0.208	1.827
Mesh 4	0.344	0.207	0.595
Mesh 5	0.344	0.207	0.000
Mesh 6	0.344	0.207	0.000

Table 2 illustrates that beyond Mesh 4, further refinement does not influence simulation results, which indicates that Mesh 4 is the optimal configuration. This grid was therefore selected for subsequent test cases and validation studies. Additionally, the results revealed that the energy yield reached a near-steady state after four turbine rotations, similar to the findings reported in [14, 17, 42, 48]. Therefore, test case simulations were conducted for five rotations to ensure convergence and accuracy.

3.3.2 Time Step Independence Analysis for SHT Simulations

The time step independence study evaluates the impact of time step size on simulation accuracy and computational efficiency. This study determined an optimal time step by systematically reducing the step size while keeping all other simulation parameters constant. The initial simulations were performed for the SHT having straight blades at a TSR of 0.71 with the time step defined based on the turbine's rotation angle per step. To assess the generality of this time step selection across different twisted blade geometries, an additional simulation was conducted for the SHT with a 75° twist angle at a TSR of 0.9. Table 3 presents the obtained C_T values and the corresponding discrepancies for both turbines across the tested time steps.

Table 3 Time Step Independence Study Results: C_T Values

SHT having straight blades at 0.71 TSR			
Time Step	**Actual Time (s)**	C_T	**Discrepancy (%)**
3º	0.011520	0.356	
2º	0.007680	0.334	6.179
1º	0.003840	0.326	2.365
0.5º	0.001920	0.326	0.000
SHT having 75° twisted blades at 0.90 TSR			
Time Step	**Actual Time (s)**	C_T	**Discrepancy (%)**
3º	0.009090	0.245	
2º	0.006060	0.260	6.122
1º	0.003030	0.275	5.770
0.5º	0.001515	0.274	0.364

Results showed no significant changes in C_T below a 1°-time step, making it the optimal choice for subsequent simulations. This step size balances accuracy and computational efficiency, ensuring convergence while capturing transient dynamics.

3.4 Validation of the Numerical Model of the SHT

This section compares the simulation results with experimental data from [41] to evaluate the accuracy, reliability, and predictive capabilities of the developed numerical model. To strengthen the validation, an additional analysis compares streamlines and velocity vectors obtained from the numerical model with data from two experimental studies by [33, 35], which provide PIV and PTV measurements. Although these studies involve turbines with different designs, the comparisons help to demonstrate the numerical model's ability to replicate critical flow characteristics observed in experimental study.

3.4.1 Validation of the CFD Model Using C_P

The validation simulations retained the previously established numerical model parameters, including mesh sizes, time step, and solver settings. The boundary conditions applied to the computational domain are illustrated in Figure 9.

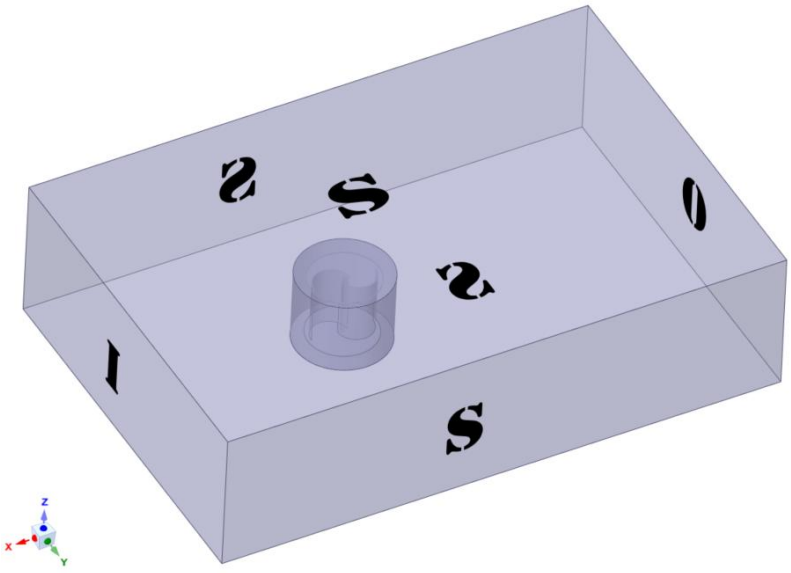

Fig. 9 Illustration of Boundary Conditions for the Computational Domain

Symmetry conditions were applied to the top, bottom, and lateral boundaries consistent with previous studies in the literature [31, 39, 49, 52, 53], and the inlet and outlet were assigned velocity-inlet and pressure-outlet conditions, respectively. While applying symmetry at the top boundary effectively mimics a simplified free surface condition, this approach does not capture the effects of varying immersion depths or detailed free surface interactions. The inlet velocity was specified based on the experimental conditions described by [41], and gravitational acceleration was applied in the negative z-direction to reflect the vertical turbine orientation. As the reference study did not provide information on the inlet turbulence intensity, a value of 5 % was assigned in this study. This choice is in line with values commonly used in previous numerical simulations of SHTs [14, 15, 20, 23]. Table 4 presents the C_P values obtained from numerical analysis and experimental measurements. In addition, Figure 10 visualizes the performance curves, including further experimental data points to illustrate the alignment between the numerically predicted and experimentally observed trends.

Table 4 Validation Results: Numerical vs. Experimental C_P Values

TSR	Experimental Results (C_P)	Numerical Results (C_P)	Difference (%)
0.60	0.220	0.207	6.1
0.71	0.250	0.232	7.4
0.80	0.253	0.243	3.8
0.86	0.261	0.250	4.2
0.91	0.244	0.246	0.9
0.98	0.240	0.245	2.1
1.10	0.170	0.163	4.2

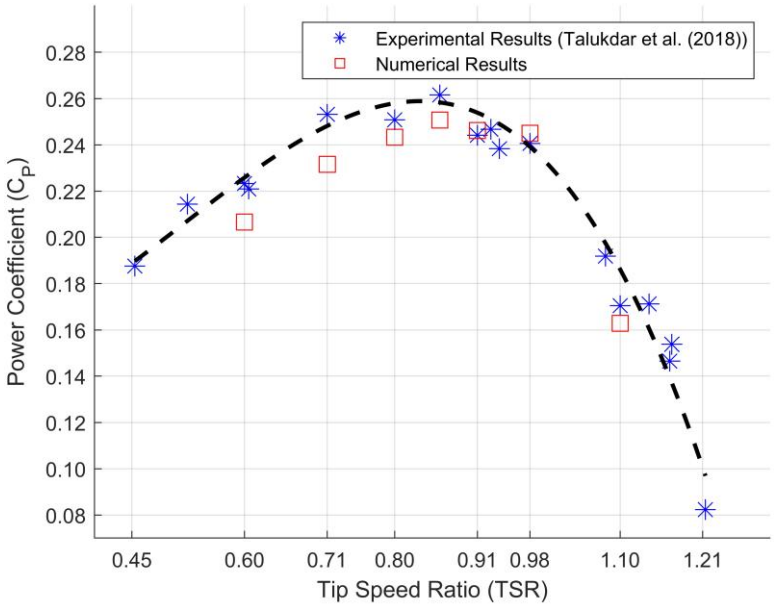

Fig. **10** Comparison of Experimental Results and Numerical Results (C_P)

As indicated by Table 4 and Figure 10, the numerical results demonstrate good agreement with the experimental study, with a maximum difference of 7.4 % at TSR 0.71 and a minimum difference of 0.9 % at TSR 0.91.

3.4.2 Comparison of Flow Fields: Numerical Model vs. Experimental Studies

PIV and PTV measurements are needed to capture velocity fields and flow patterns, however the validation research did not employ these. This constraint was addressed by comparing the numerical model

results to PIV and PTV data from two experimental investigations [33, 35]. Despite turbine design variances in the compared studies, this comparison aims to show the numerical model's ability to capture key flow dynamics and to validate its predictive reliability.

Fujisawa [33] studied a SHT having an OR of 0.15, operating at a TSR of 0.9 in a water channel. Due to insufficient inlet velocity for natural rotation, the turbine was artificially driven at this TSR in the experiments. Phase-averaged velocity vectors were obtained using PIV data and presented in Figure11(a). For comparison, the numerical model results at TSR 0.9 obtained by generating instantaneous velocity vectors are presented in Figure11(b).

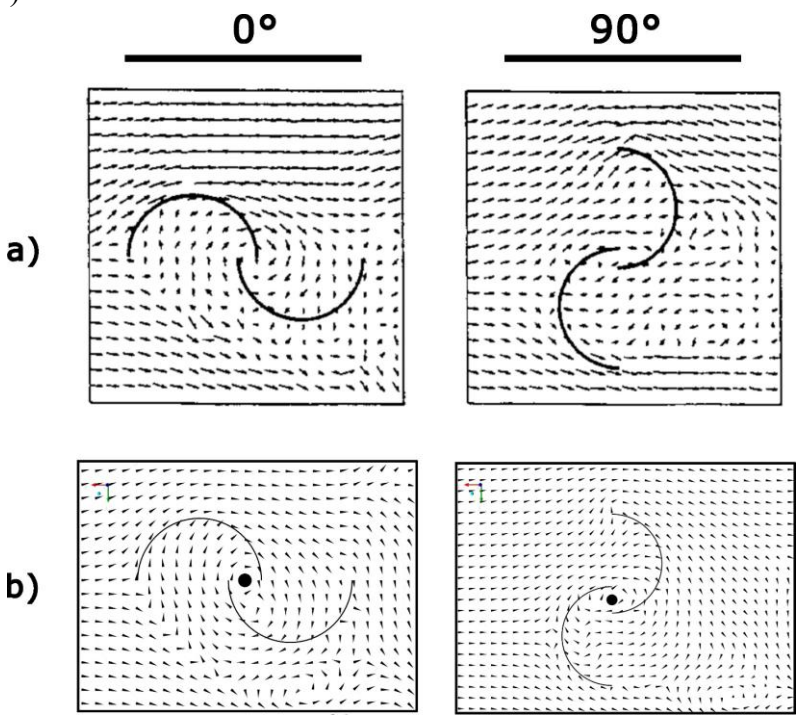

Fig. 11 Velocity vectors provided by Fujisawa [33] for TSR 0.9 (a), velocity vectors obtained from the developed CFD model at TSR 0.9 (b)

The numerical model successfully reproduced key flow features, including wall-attached flow on the convex side of the advancing blade and flow separation on the convex side of the returning blade. However, it did not fully capture the vortex formation behind the advancing blade at 90°, consistent with the known limitations of RANS SST *k-ω* models in resolving such structures [31]. Differences in recirculating flow at the blade gap were attributed to the inclusion of the shaft in the numerical model, which is absent in the experimental setup.

Murai et al. [35] analyzed flow fields around an SHT having an OR of 0.16, operating at a TSR of 0.5 in a water channel. PTV data collected from 15 turbine rotations were used to generate phase-average streamlines (Figure 12(a)). The numerical model was run at the same TSR of 0.5 to produce comparable streamlines in a stationary reference frame (Figure 12(b)).

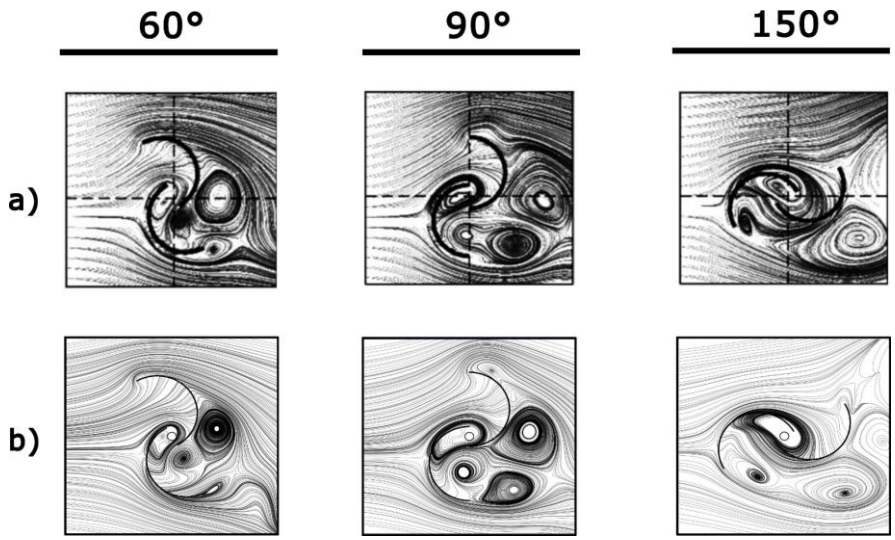

Fig. 12 Streamlines provided by Murai et al. [35] for TSR 0.5 (a), streamlines generated from the developed CFD model at TSR 0.5 (b)

The numerical model closely matched the experimental streamlines, replicating vortex formations and flow separation patterns observed in the results of Murai et al. [35]. At this lower TSR, the model effectively captured additional vortex structures arising from pronounced flow separation over the convex side of the advancing blade, which were not observed in comparison with the study of Fujisawa [33].

4. Results

In this section, the results of the investigation on the impact of blade twist angle on the performance of Helical SHTs (HSHT) are presented. Blade twist angles ranging from 0° to 90° are considered to generate helical blade profiles, with the corresponding HSHT geometries illustrated in Figure 13. The twisted blade geometries were generated by defining a helical path specific to each blade twist angle and sweeping the cross-sectional profile of the baseline SHT along this path. The configuration with a blade twist angle of 0° represents the benchmark SHT for comparison in the analysis. Figure 13 provides the test IDs assigned to each configuration. These IDs will be used throughout the results section to refer to the respective turbine models for clarity and consistency.

In the CFD simulations, the geometric parameters of both the Rotational Domain and Static Domain remain unchanged across all test cases. While the blade geometry of the SHT varied, other design factors were held constant.

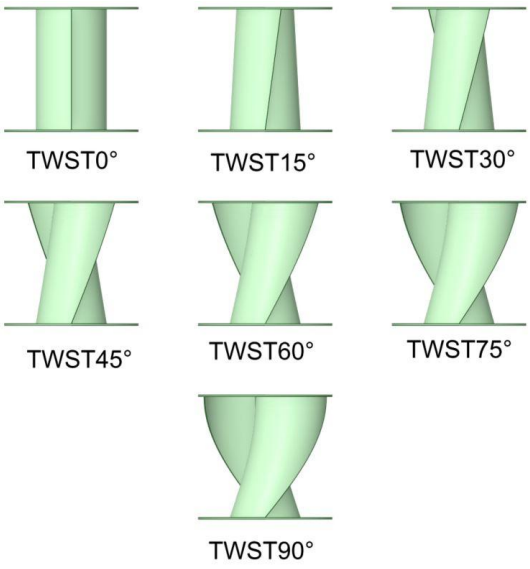

Fig. 13 Generated HSHT geometries

4.1 Performance Analysis of Helical Blade Profiles

The performance data obtained of the helical configurations with blade twist angles ranging from 0° to 90° are compared to each other for TSRs ranging from 0.6 to 1.1. The average C_T variation for the TSR range under consideration is illustrated in Figure 14 for all blade twist angles that have been analyzed.

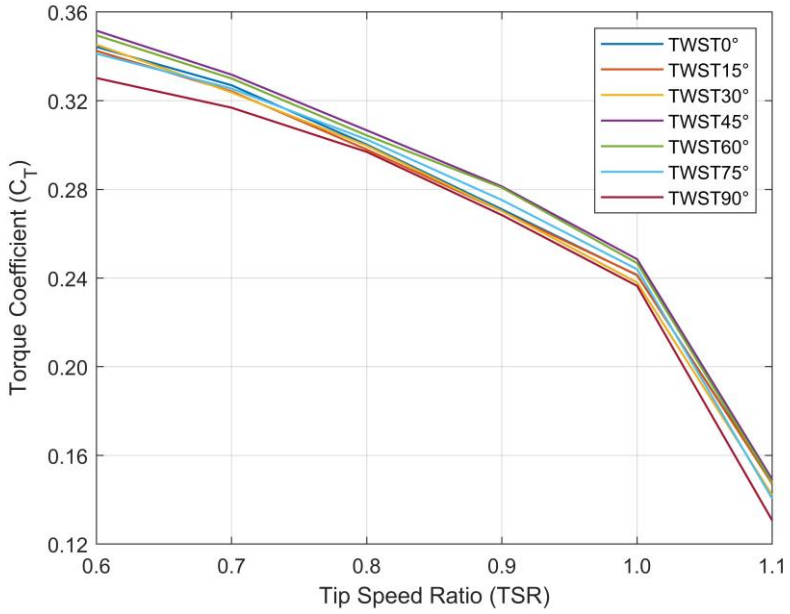

Fig. 14 C_T vs. TSR curves of HSHT configurations

Figure 14 shows that the highest C_Ts are produced at a TSR of 0.6 for all blade twist angles investigated. With an increase in TSR, the average C_Ts generated by all helical configurations decrease dramatically, particularly at TSR 1.1. The highest C_T is obtained with a blade twist angle of 45°, resulting in a value of 0.352 at a TSR of 0.6. This value is 2.12 % greater than the C_T attained with a blade twist angle of 0°. Moreover, TWST45° achieved the highest C_Ts at all TSR values. To better visualize the change of exhibited C_Ts by the different blade angles, Figure 15 displays the produced average C_T values for the TSRs under study over phase difference angles.

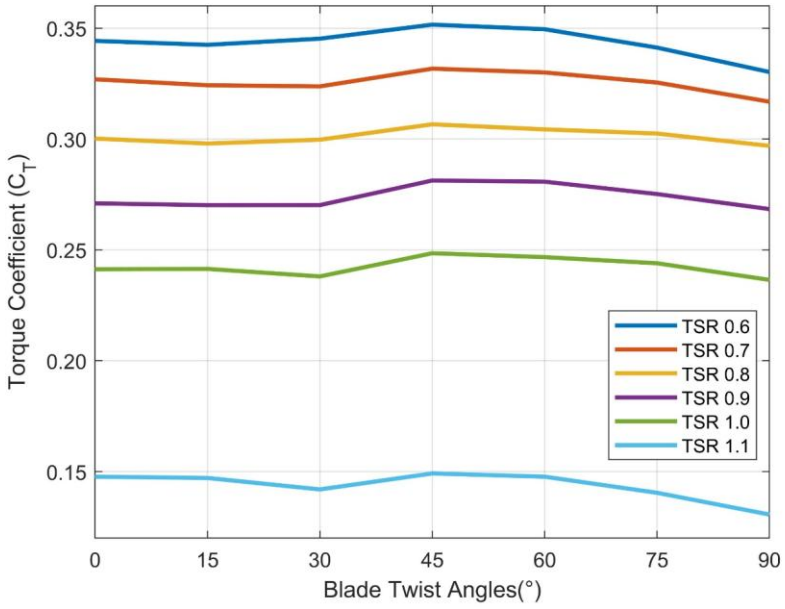

Fig. 15 C_T vs. blade twist angle curves of HSHT configurations

The presented C_T versus twist angle curves in Figure 15 exhibit similar trends across the presented TSRs. TWST15° and TWST30° achieve nearly identical C_T values similar to TWST0° for all considered TSRs. It is noteworthy that TWST0° attains slightly higher C_Ts than TWST15° and TWST30° at all TSRs, except for TSR 0.6, where TWST30° generates a higher C_T than TWST0°. While TWST45° and TWST60° generate comparable C_Ts, the torque generation capacity of the studied configurations consistently peaks at a blade twist angle of 45° across all TSRs. It is worth emphasizing that the maximum improvement offered by TWST45° over TWST60° is a modest 1 % at TSR 1.1. Beyond a blade twist angle of 60°, the torque generation capacity gradually decreases with the lowest C_Ts consistently generated by TWST 90°. Figure 16 illustrates the variation in average C_P across all blade twist angles for the considered TSRs.

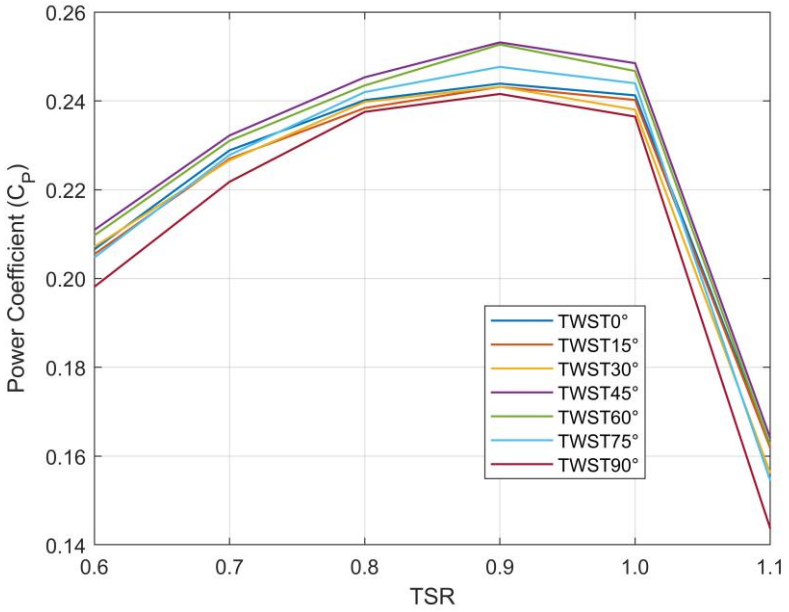

Fig. 16 C_P vs. blade twist angle curves of HSHT configurations

The peak C_Ps are generated at a TSR of 0.9 by all studied helical configurations, as displayed in Figure 16. The maximum C_P generated is 0.252 at 0.9 TSR by TWST45°, which is 3.81 % higher than that of TWST0°. TWST45° also generates the highest C_Ps at all TSRs among the considered blade twist angles. Notably, TWST45° and TWST60° generate comparable C_Ps for all TSRs, especially for 0.9 TSR. The lowest C_Ps are consistently generated by TWST90° at all TSRs. As illustrated in Figure 16, TWST0°, TWST15° and TWST30° show closely aligned C_P values at all TSRs. It is acknowledged that additional TSR data points near the peak would allow a more precise evaluation of potential shifts in optimal TSR due to twist; however, due to computational constraints, the current resolution was selected to balance accuracy and feasibility. Moreover, while the present study thoroughly investigates multiple twist configurations, it does not include intermediate twist angles between 45° and 60°, which may provide further performance insights. Future work may aim to explore these intermediate geometries and incorporate finer TSR sampling near the peak region to offer a more detailed characterization of performance trends induced by blade twist. Figure 17 illustrates the torque generation curves of turbines with different blade twist angles during a single rotation of each turbine at TSR 0.9 in terms of generated torque (Nm).

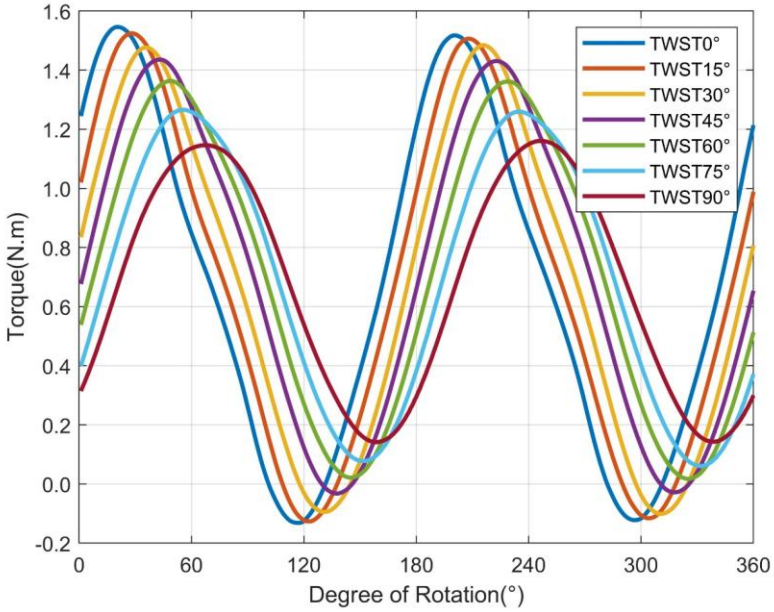

Fig. 17 Torque generated by HSHT configurations over a single rotation at TSR 0.9

As presented in Figure 17, the oscillations observed on the torque generated are significantly reduced. The standard deviation of TWST90°'s torque profile is 35.21 % less compared to that of TWST0°. Although TWST45° achieved slightly better performance than TWST60°, TWST60° exhibits 7.28 % less torque fluctuations compared to TWST45°.

The reduction in torque fluctuations achieved using helical blade profiles may contribute to mitigating mechanical vibrations, mechanical loads, and noise emissions. These reductions could potentially enhance the structural integrity of the turbine by lowering the risk of fatigue or structural failure. Furthermore, decreased torque fluctuations are likely to alleviate the stress on voltage regulation systems coupled with the turbine, potentially improving operational stability and reliability. This reduction in electrical component strain may also support a modest improvement in the overall efficiency of the system.

4.2 Comparison with Literature on Optimal Twist Angles

The present study identifies a twist angle of 45° (TWST45°) as the most efficient configuration, achieving the highest power coefficient ($C_P = 0.252$) at a tip speed ratio (TSR) of 0.9. This finding is in strong agreement with previous studies on SWTs, including those of Lee et al. [22], El-Askary et al. [23], and Saad et al. [24], which also reported optimal performance at a 45° twist angle. Notably, while El-Askary et al. [23] and Saad et al. [24] observed maximum C_P values of 0.220 and 0.194, respectively, at TSR = 0.8, Lee et al. [22] reported a lower peak C_P of 0.130 at TSR = 0.54. These results are broadly consistent with the current findings, suggesting a robust performance enhancement associated with moderate twist angles. In contrast, Rengma et al. [21] reported significantly different results for SHTs, identifying 120° as the optimal twist angle with a corresponding C_P of 0.19 at TSR = 0.8. Interestingly, this angle was among the least efficient in the aforementioned SWT studies, where C_P values dropped significantly beyond 90° of twist. This inconsistency may be attributed to differences in test conditions.

The present study also highlights the effectiveness of a 60° twist angle, which emerged as the second-best performer ($C_P = 0.250$ at TSR = 0.9). Patel et al. [19] also tested an SHT with 60° twisted blades and reported a similar C_P of 0.2434 at TSR = 0.884, providing further support for the present findings in a hydrokinetic setting. Notably, the 60° twist angle was also included in the studies of El-Askary et al. [23] and Rengma et al. [21], though with contrasting results. While El-Askary et al. [23] ranked it as the third-best configuration ($C_P = 0.212$ at TSR = 0.8), Rengma et al. [21] reported it among the lowest-performing designs.

These observed inconsistencies, both between SWT and SHT studies and in the performance evaluations of the 60° twist angle, underscore the complex interplay between blade geometry, flow medium, and testing

conditions. They further emphasize the need for systematic and consistent investigations of twisted blade geometries specifically tailored for hydrokinetic turbine applications.

4.3 Discussion on the flow field around helical turbines

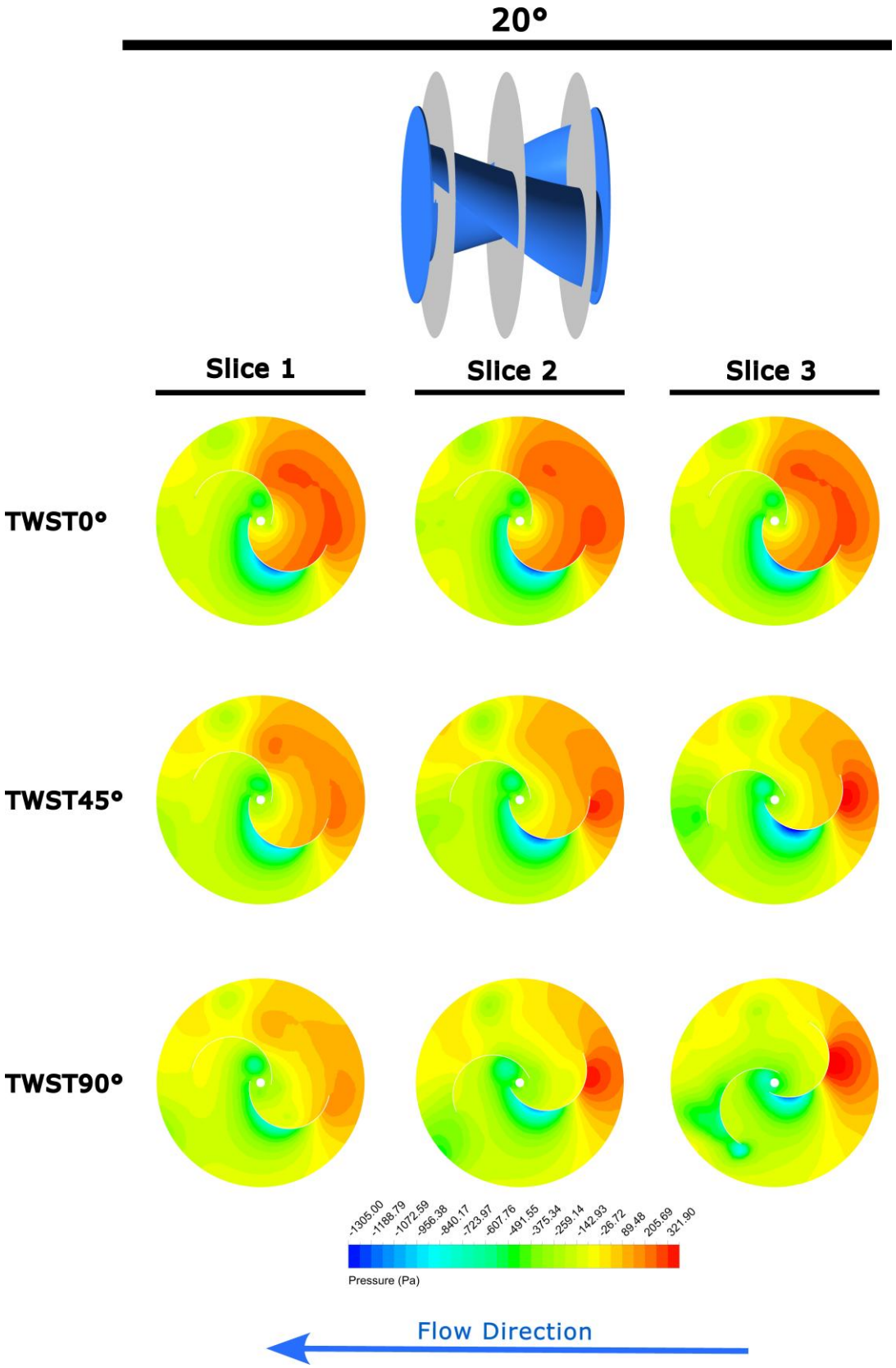

Fig. 18 Pressure contours along the length of TWST0°, TWST45° and TWST90° at 20° of rotation and 0.9 TSR

The twisted blade profiles in a HSHT create a continuous phase difference in the orientation of the blades along the length of the SHT. This continuous phase difference helps HSHT distribute torque generation along the length of the blades, thereby reducing torque fluctuations as illustrated in Figure 17. To better understand this effect, the pressure contours around the blades of TWST0°, TWST45° and TWST90° are presented at 20° of rotation in Figure 18. Specifically, the pressure contours are presented at three different locations along the length of the turbines. These locations are depicted in Figure 18 and named Slice 1, Slice 2, and Slice 3.

TWST0° has straight blades; therefore, the azimuth angles of the blade cross-sections are constant at 20° along the turbine length as can be seen in Figure 13 and Figure 4. On the other hand, the azimuth angles of the blade cross-sections in TWST45° and TWST90° continuously decrease due to the applied blade twist, as can be seen by comparing the provided contours at slices in Figure 18. At 20° of rotation, the cross-section of blades in Slice 1 of TWST45° and TWST90° are slightly lower than 20° as Slice 1 is generated just ahead of the endplate where the blades' cross-sections are at 20°.

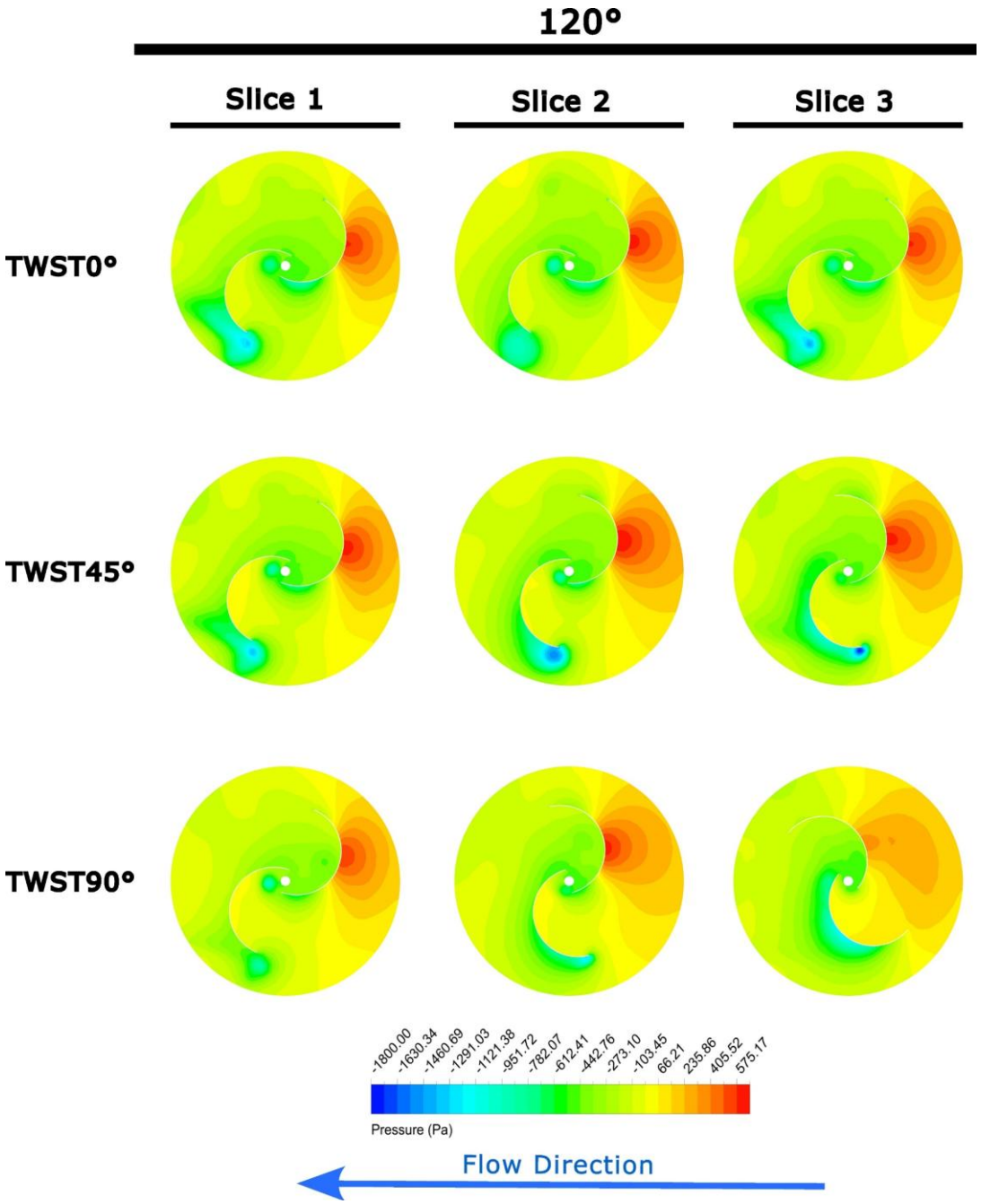

Fig. 19 Pressure contours along the length of TWST0°, TWST45° and TWST90° at 120° of rotation and 0.9 TSR

As shown in Figure 18, the pressure over the concave side of TWST0°'s advancing blade is much higher than TWST45° and TWST90° at Slice 1 where the blade sections are at similar azimuth angles. At Slice 2, which presents the middle-sections of the turbines, the cross-sections presented for TWST90° and TWST45° are at significantly lower azimuth angles compared to that of Slice 1 due to phase shift. Therefore, the incoming water first impacts the convex side of the returning blades of TWST45° and TWST90°. As a result, the torque generation capacity of TWST45° and TWST90° is decreased. In contrast, the cross-section of TWST0° is exactly at 20°. The same observation can also be made for Slice 3 where the presented pressure contours are compared to each other, the high-pressure zones occur at the convex side of the returning blades of TWST45° and TWST90°. Therefore, the torque generation capacity of TWST45° and TWST90° is significantly reduced along the lengths of the turbines.

At 20°, TWST0° achieves maximum instantaneous torque and a higher torque value than TWST45° and TWST90°, as illustrated in Figure 17. Moreover, at 20°, TWST45° exhibits a higher torque value compared to TWST90° as seen in Figure 17, due to a lower phase difference angle than TWST90°. When the presented pressure contours of TWST45° and TWST90° at Slice 2 and Slice 3 are compared, it can be seen that the pressure on the convex side of the returning blade is higher for TWST90°. Therefore, TWST90° experiences greater negative torque compared to TWST45°. Figure 19 illustrates the pressure contours of TWST0°, TWST45° and TWST90° at 120° of rotation for the same slice locations as Figure 18.

At 120° of rotation, the convex side of the returning blade is positioned in front of the advancing blade. Therefore, the incoming water flow first impacts on the convex side of the returning blades and creates significant negative torque on the SHT. The returning blade also partially shields the advancing blade from the water flow at 120°. As a result, at 120°, a significant reduction in the torque generation capacity of the cross-section of SHT occurs. As seen in Slice 1 in Figure 19, the presented pressure contours are very similar to each other, even though the pressure on TWST45°'s returning blade is slightly higher than that of the others. When the pressure contours at Slice 2 are compared, the pressure over the concave side of the advancing blade increases as the twist angle becomes larger, while the pressure on the convex side of the returning blades remain similar. Consequently, at the middle of the turbines, TWST45° and TWST90°'s advancing blades generate higher positive torque compared to TWST0°. As can be seen in Figure 19, the cross-section of TWST90° presented at Slice 3 is around 30° due to a 90° twist angle. Therefore, the advancing blade of TWST90° is positioned in front of the returning blade. Consequently, the pressure on the advancing blade of TWST90° is much higher compared to TWST0°. Also, the pressure on the convex side of TWST90°'s returning blade is significantly lower than TWST0°. Furthermore, the cross-section presented for TWST45° at Slice 3 is at an azimuth angle of 85°, where standard SHT produces significantly higher torque compared to 120° of rotation. As a result of the observations discussed, at 120° of rotation, TWST90° exhibits higher instantaneous torque than both TWST45° and TWST90° as illustrated in Figure 17, and TWST45° also exhibits a larger torque value than TWST0° at 120°.

Figure 18 and Figure 19 show that along the turbine length, the pressure distribution is almost uniform for the TWST0°. However, the introduction of the twisted blades significantly alters the pressure distribution over the blade profile along the length of the turbine. In Figure 20, the pressure distributions over the blade profiles of TWST90°, TWST45°, and TWST0° are presented at 90° of rotation.

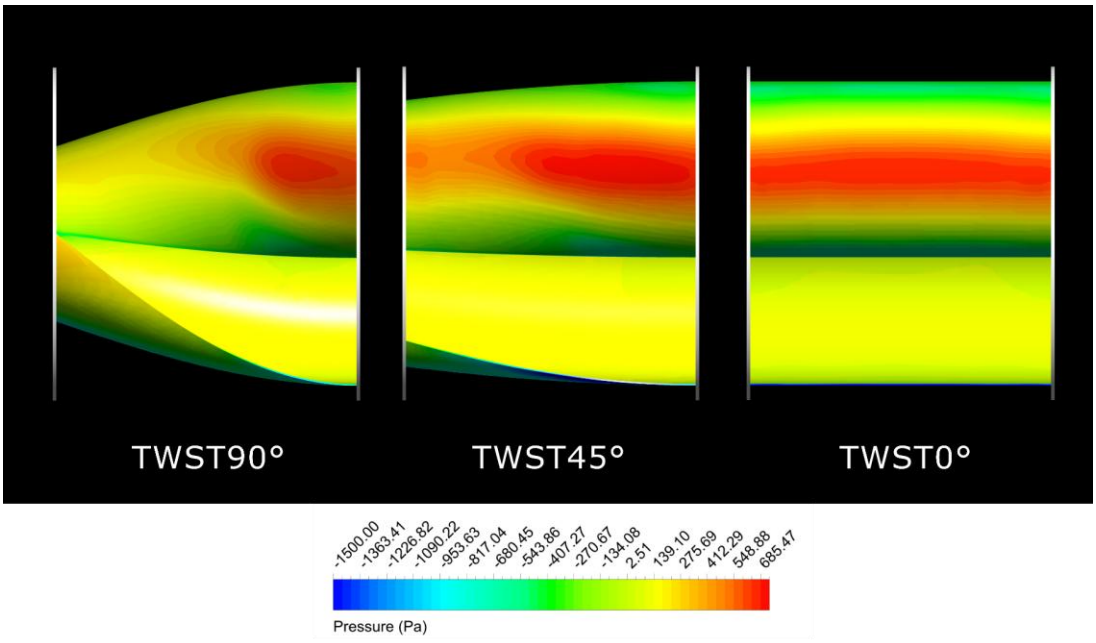

Fig. 20 Pressure distribution over the blade surfaces of TWST0°, TWST45° and TWST90° at 90° of rotation and 0.9 TSR

As shown in Figure 20, the pressure distribution on the blades of TWST0° is uniformly distributed. However, the pressure distributions on the blades of TWST90° and TWST45° gradually change along the length of the turbine. The regions closer to the right endplates of TWST45° and TWST90° are at azimuth angles closer to 90°; therefore, the pressure distribution is very similar to that of TWST0°. However, due to continuous change in azimuth angle along the blade profile, the pressure distribution gradually changes and the pressure over the left side decreases. The velocity vector distribution over the blade profiles is presented in Figure 21 to visualize the effects of gradually changing pressure distribution.

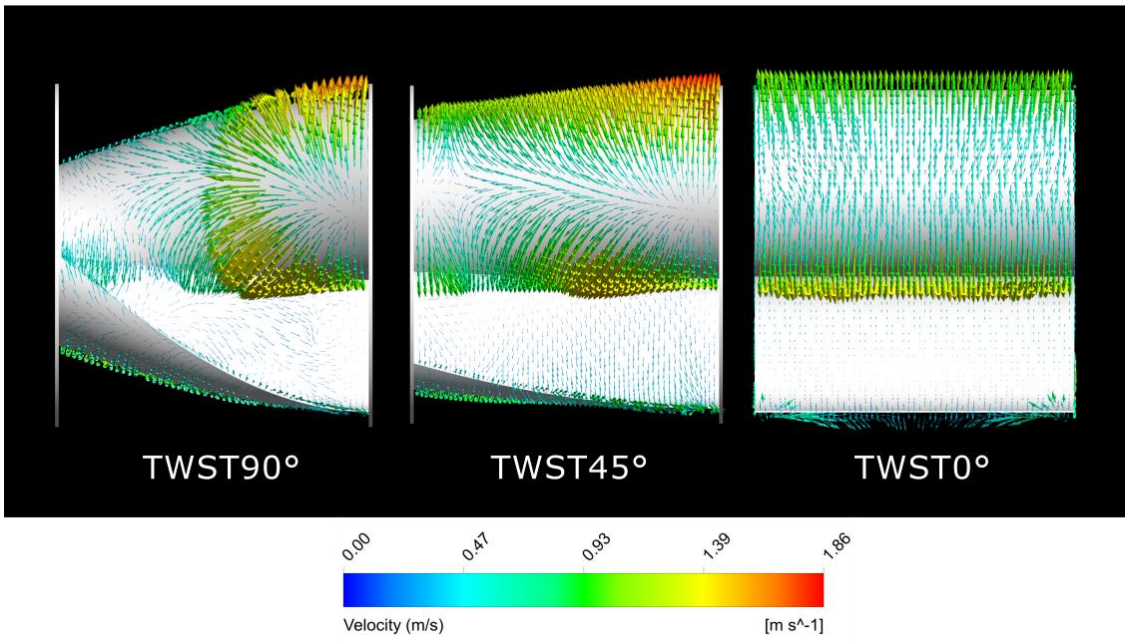

Fig. 21 Velocity field over the blade surfaces of TWST0°, TWST45° and TWST90° at 90° of rotation and 0.9 TSR. The vectors represent the velocity field in the stationary reference frame.

The uniform pressure distribution observed on TWST0°'s blades forces the incoming flow into a more planar motion as seen in Figure 21, where the velocity vectors presented for TWST0° move perpendicularly to the incoming velocity vector and parallel to the blade surface. On the other hand, the velocity vectors of TWST45° and TWST90° indicate that some portion of the incoming water from the right side of the turbine,

where high pressure occurs, is directed towards the left side of the turbine, where a lower pressure zone is observed. Due to the gradual shift in pressure distribution, the incoming flow follows a swirling path along the blade profiles. As a result, some portion of the high energy incoming flow is redistributed towards the low-pressure zone, which increases the utilization of the incoming flow and improves efficiency.

5. Conclusions

This study systematically investigated the effects of twisted blade profiles on the performance of the studied SHT using CFD. The research fills a notable gap in the literature by methodically investigating a broader range of blade twist angles (15°, 30°, 45°, 60°, 75°, 90°) and offers valuable insights into the optimization of SHT designs. The results provide a strong foundation for future studies on advanced turbine configurations.

The findings highlight the significant potential of twisted blades to enhance SHT performance by addressing the inherent limitations of conventional designs. The SHT with a blade twist angle of 45°, exhibited the highest performance among the tested configurations, achieving a C_P of 0.252. This C_P value corresponds to a 3.81 % improvement compared to the SHT with conventional blades. Furthermore, it showed a considerable reduction in torque fluctuations by exhibiting 9.38 % less variability compared to the conventional design, which contributes to operational stability. Interestingly, the SHT with a 60° blade twist angle produced similar but slightly lower C_P values across all TSRs, with only marginal differences in performance compared to the SHT with a 45° blade twist. Moreover, it exhibited a further reduction in torque fluctuations, by decreasing them by 7.28 % compared to the SHT with a 45° blade twist. This suggests that the 60° blade twist angle could serve as an alternative to mitigate operational challenges, particularly for applications prioritizing torque stability. Additionally, flow visualization techniques were employed to investigate the flow field around the twisted blade configurations. The inclusion of twisted blades was found to create a gradually changing pressure distribution along the blades span which redirects incoming flow to the low-pressure zone and enhances the utilization of incoming flow energy.

ACKNOWLEDGMENTS

This work was supported by METU Scientific Research Project Department, [grant no: GAP-303-2022-10895], project title “Hydrokinetic Turbine Design – Operates Efficiently at Low Velocity Flows”.

REFERENCES

[1] IEA International Energy Agency, 2019. Africa Energy Outlook 2019. World Energy Outlook Special Report. *EA Publications*. 288.

[2] Paish, O., 2002. Small Hydro Power: Technology and Current Status. *Renewable and Sustainable Energy Reviews*, *6*, 537-556. https://doi.org/10.1016/S1364-0321(02)00006-0

[3] Behrouzi, F., Nakisa, M., Maimun, A., Ahmed, Y. M., 2016. Global Renewable Energy and Its Potential in Malaysia: A Review of Hydrokinetic Turbine Technology. *Renewable and Sustainable Energy Reviews*, *62*, 1270-1281. https://doi.org/10.1016/j.rser.2016.05.020

[4] Fraenkel, P. L., 2007. Marine Current Turbines: Pioneering the Development of Marine Kinetic Energy Converters, *Proceedings of the Institution of Mechanical Engineers Part A Journal of Power and Energy*, 221, 159-169. https://doi.org/10.1243/09576509JPE307

[5] Sood, M.; Singal, S. K., 2019. Development of Hydrokinetic Energy Technology: A Review. *International Journal of Energy Research*, 43, 5552-5571. https://doi.org/10.1002/er.4529

[6] U.S Department of Energy Quadrennial Technology Review, 2015. Marine and Hydrokinetic Power - Chapter 4: Technology Assessments. *Quadrennial Technology Review*.

[7] Khan, M. J., Bhuyan, G., Iqbal, M. T., Quaicoe, J. E., 2009. Hydrokinetic Energy Conversion Systems and Assessment of Horizontal and Vertical Axis Turbines for River and Tidal Applications: A Technology Status Review. *Applied Energy*, 86, 1823-1835. https://doi.org/10.1016/j.apenergy.2009.02.017

[8] Kumar, A., Saini, R. P., 2016. Performance Parameters of Savonius Type Hydrokinetic Turbine – A Review. *Renewable and Sustainable Energy Reviews*, 64, 289-310. https://doi.org/10.1016/j.rser.2016.06.005

[9] Maldar, N. R., Ng, C. Y., Oguz, E., 2020. A Review of the Optimization Studies for Savonius Turbine Considering

Hydrokinetic Applications. *Energy Conversion and Management*, 226, 113495. https://doi.org/10.1016/j.enconman.2020.113495

[10] Yadav, P. K., Kumar, A., Jaiswal, S., 2023. A Critical Review of Technologies for Harnessing the Power from Flowing Water Using a Hydrokinetic Turbine to Fulfill the Energy Need. *Energy Reports*, 9, 2102-2117. https://doi.org/10.1016/j.egyr.2023.01.033

[11] Badrul Salleh, M., Kamaruddin, N. M., Mohamed-Kassim, Z., 2019. Savonius Hydrokinetic Turbines for a Sustainable River-Based Energy Extraction: A Review of the Technology and Potential Applications in Malaysia. *Sustainable Energy Technologies and Assessments*, 36, 100554. https://doi.org/10.1016/j.seta.2019.100554

[12] Modi, V. J., Fernando, M. S. U. K., 1989. On the Performance of the Savonius Wind Turbine. *Journal of Solar Energy Engineering, Transactions of the ASME*, 111, 71-81. https://doi.org/10.1115/1.3268289

[13] Zullah, M. A., Prasad, D., Choi, Y. D., Lee, Y. H., 2010. Study on the Performance of Helical Savonius Rotor for Wave Energy Conversion. *In Proceedings of the AIP Conference Proceedings*, 1225, 641-649. https://doi.org/10.1063/1.3464913

[14] Kumar, A., Saini, R. P., 2017. Performance Analysis of a Savonius Hydrokinetic Turbine Having Twisted Blades. *Renewable Energy*, 108, 502-522. https://doi.org/10.1016/j.renene.2017.03.006

[15] Kumar, A., Saini, R. P., 2017. Performance Analysis of a Single Stage Modified Savonius Hydrokinetic Turbine Having Twisted Blades. *Renewable Energy*, 113, 461-478. https://doi.org/10.1016/j.renene.2017.06.020

[16] Hadi, S., Sidiq, M., Cahyo Anindito, D., Prasetyo, A., Danardono, D., Prija Tjahjana, D., et al., 2019. Experimental Study of The Effects of Blade Twist on the Performance of Savonius Water Turbine in Water Pipe. *Journal of Advanced Research in Fluid Mechanics and Thermal Sciences*, 57, 202-207.

[17] Mosbahi, M., Ayadi, A., Chouaibi, Y., Driss, Z., Tucciarelli, T., 2019. Performance Study of a Helical Savonius Hydrokinetic Turbine with a New Deflector System Design. *Energy Conversion and Management*, 194, 55-74. https://doi.org/10.1016/j.enconman.2019.04.080

[18] Mosbahi, M., Elgasri, S., Lajnef, M., Mosbahi, B., Driss, Z., 2021. Performance Enhancement of a Twisted Savonius Hydrokinetic Turbine with an Upstream Deflector. *International Journal of Green Energy*, 18, 51-65. https://doi.org/10.1080/15435075.2020.1825444

[19] Patel, V., Patel, C., 2022. Performance Investigation of Twisted Blade Inline Savonius Turbine at Variable Load Condition Using Numerical Method. *Materials Today: Proceedings*, 49, 250-256. https://doi.org/10.1016/j.matpr.2021.01.868

[20] Nag, A. K., Sarkar, S., 2020. Experimental and Numerical Study on the Performance and Flow Pattern of Different Savonius Hydrokinetic Turbines with Varying Duct Angle. *Journal of Ocean Engineering and Marine Energy*, 6, 31-53. https://doi.org/10.1007/s40722-019-00155-6

[21] Rengma, T. S., Subbarao, P. M. V., 2025. Studies on Role of Twist Angle on Performance of Savonius Hydrokinetic Turbine Variants. *Renewable Energy*, 241, 122303. https://doi.org/10.1016/j.renene.2024.122303

[22] Lee, J. H., Lee, Y. T., Lim, H. C., 2016 Effect of Twist Angle on the Performance of Savonius Wind Turbine. *Renewable Energy*, 89, 231-244. https://doi.org/10.1016/j.renene.2015.12.012

[23] El-Askary, W. A., Saad, A. S., Abdel Salam, A. M., Sakr, I. M., 2018. Investigating the Performance of a Twisted Modified Savonius Rotor. *Journal of Wind Engineering and Industrial Aerodynamics*, 182, 344-355. https://doi.org/10.1016/j.jweia.2018.10.009

[24] Saad, A. S., El-Sharkawy, I. I., Ookawara, S., Ahmed, M., 2020. Performance Enhancement of Twisted-Bladed Savonius Vertical Axis Wind Turbines. *Energy Conversion and Management*, 209, 112673. https://doi.org/10.1016/j.enconman.2020.112673

[25] Damak, A., Driss, Z., Abid, M. S., 2013. Experimental Investigation of Helical Savonius Rotor with a Twist of 180°. *Renewable Energy*, 52, 136-142. https://doi.org/10.1016/j.renene.2012.10.043

[26] Kamoji, M. A., Kedare, S. B., Prabhu, S. V., 2009. Performance Tests on Helical Savonius Rotors. *Renewable Energy*, 34, 521-529. https://doi.org/10.1016/j.renene.2008.06.002

[27] Saha, U. K., Rajkumar, M. J., 2006. On the Performance Analysis of Savonius Rotor with Twisted Blades. *Renewable Energy*, 31, 1776-1788. https://doi.org/10.1016/j.renene.2005.08.030

[28] Abdelsalam, A. M., Kotb, M. A., Yousef, K., Sakr, I. M., 2021. Performance Study on a Modified Hybrid Wind Turbine with Twisted Savonius Blades. *Energy Conversion and Management*, 241, 114317. https://doi.org/10.1016/j.enconman.2021.114317

[29] Sarma, N. K., Biswas, A., Misra, R. D., 2014. Experimental and Computational Evaluation of Savonius Hydrokinetic Turbine for Low Velocity Condition with Comparison to Savonius Wind Turbine at the Same Input Power. *Energy Conversion and Management*, 83, 88-98. https://doi.org/10.1016/j.enconman.2014.03.070

[30] Talukdar, P. K., Kulkarni, V., Saha, U. K., 2018. Performance Estimation of Savonius Wind and Savonius Hydrokinetic Turbines under Identical Power Input. *Journal of Renewable and Sustainable Energy*, 10, 064704. https://doi.org/10.1063/1.5054075

[31] Dobrev, I., Massouh, F., 2011. CFD and PIV Investigation of Unsteady Flow through Savonius Wind Turbine. *Energy*

Procedia, 6, 711-720. https://doi.org/10.1016/j.egypro.2011.05.081

[32] Fujisawa, N., Gotoh, F., 1992. Visualization Study of the Flow in and around a Savonius Rotor. *Experiments in Fluids*, 12, 407-412. https://doi.org/10.1007/BF00193888

[33] Fujisawa, N., 1996 Velocity Measurements and Numerical Calculations of Flow Fields in and around Savonius Rotors. *Journal of Wind Engineering and Industrial Aerodynamics*, 59, 39-50. https://doi.org/10.1016/0167-6105(94)00031-X

[34] Shigetomi, A., Murai, Y., Tasaka, Y., Takeda, Y., 2011. Interactive Flow Field around Two Savonius Turbines. *Renewable Energy*, 36, 536-545. https://doi.org/10.1016/j.renene.2010.06.036

[35] Murai, Y., Nakada, T., Suzuki, T., Yamamoto, F., 2007. Particle Tracking Velocimetry Applied to Estimate the Pressure Field around a Savonius Turbine. *Measurement Science and Technology*, 18, 2491. https://doi.org/10.1088/0957-0233/18/8/026

[36] Menter, F. R., 1994. Two-Equation Eddy-Viscosity Turbulence Models for Engineering Applications. *AIAA Journal*, 32, 1598-1605. https://doi.org/10.2514/3.12149

[37] Menter, F. R., 1992. Improved Two-Equation k-Omega Turbulence Models for Aerodynamic Flows. *NASA Technical Memorandum*, 103975. https://doi.org/10.2514/6.1993-2906

[38] Nasef, M. H., El-Askary, W. A., AbdEL-hamid, A. A., Gad, H. E., 2013. Evaluation of Savonius Rotor Performance: Static and Dynamic Studies. *Journal of Wind Engineering and Industrial Aerodynamics*, 123, 1-11. https://doi.org/10.1016/j.jweia.2013.09.009

[39] Ferrari, G., Federici, D., Schito, P., Inzoli, F., Mereu, R., 2017. CFD Study of Savonius Wind Turbine: 3D Model Validation and Parametric Analysis. *Renewable Energy*, 105, 722-734. https://doi.org/10.1016/j.renene.2016.12.077

[40] Alom, N., Saha, U. K., Dewan, A., 2021. In the Quest of an Appropriate Turbulence Model for Analyzing the Aerodynamics of a Conventional Savonius (S-Type) Wind Rotor. *Journal of Renewable and Sustainable Energy*, 13, 023313. https://doi.org/10.1063/5.0034362

[41] Talukdar, P. K., Sardar, A., Kulkarni, V., Saha, U. K., 2018. Parametric Analysis of Model Savonius Hydrokinetic Turbines through Experimental and Computational Investigations. *Energy Conversion and Management*, 158, 36-49. https://doi.org/10.1016/j.enconman.2017.12.011

[42] Shashikumar, C. M., Vijaykumar, H., Vasudeva, M., 2021. Numerical Investigation of Conventional and Tapered Savonius Hydrokinetic Turbines for Low-Velocity Hydropower Application in an Irrigation Channel. *Sustainable Energy Technologies and Assessments*, 43, 100871. https://doi.org/10.1016/j.seta.2020.100871

[43] M, S. C., Kadam, A. R., Parida, R. K., 2024. Numerical Studies on the Performance of Savonius Turbines for Hydropower Application by Varying the Frontal Cross-Sectional Area. *Ocean Engineering*, 306, 117922. https://doi.org/10.1016/j.oceaneng.2024.117922

[44] Torres, S., Marulanda, A., Montoya, M. F., Hernandez, C., 2022. Geometric Design Optimization of a Savonius Wind Turbine. *Energy Conversion and Management*, 262, 115679. https://doi.org/10.1016/j.enconman.2022.115679

[45] Kumar, A., Saini, R. P., 2016. Numerical Investigations on Single Stage and Multi-Stage Twisted Savonius Hydrokinetic Turbine. *Proceedings of the 6th International and 43rd National Conference on Fluid Mechanics and Fluid Power* (FMFP 2016), December 15-17, Allahabad, India, 474.

[46] Liang, L., Hao, Z., Chaonan, Z., Jinbiao, C., Baoji, Z., Xiangen, B., et al., 2024. Study on the effect of marine propeller wake on sediment siltation in a shallow water channel. *Brodogradnja*, 75, 75308. https://doi.org/10.21278/brod75308

[47] Liang, L., Zhang, B., Zhang, H., Tang, H., Wang, W., 2023. Hydrodynamic performance optimization of marine propellers based on fluid-structure coupling. *Brodogradnja*, 74(3), 145-164. https://doi.org/10.21278/brod74308

[48] Saini, G., Saini, R. P., 2020. A Computational Investigation to Analyze the Effects of Different Rotor Parameters on Hybrid Hydrokinetic Turbine Performance. *Ocean Engineering*, 199, 107019. https://doi.org/10.1016/j.oceaneng.2020.107019

[49] Maldar, N. R., Yee, N. C., Oguz, E., Krishna, S., 2022. Performance Investigation of a Drag-Based Hydrokinetic Turbine Considering the Effect of Deflector, Flow Velocity, and Blade Shape. *Ocean Engineering*, 266, 112765. https://doi.org/10.1016/j.oceaneng.2022.112765

[50] Zhang, Z., Sun, P., Pan, L., Zhao, T., 2024. On the propeller wake evolution using large eddy simulations and physics-informed space-time decomposition. *Brodogradnja*, 75(1), 75102. https://doi.org/10.21278/brod75102

[51] Liang, L., Baoji, Z., Hao, Z., Jiaye, G., Zheng, T., Shuhui, G., et al., 2024. Study on numerical simulation and mitigation of parametric rolling in a container ship under head waves. *Brodogradnja*, 75(3), 75305. https://doi.org/10.21278/brod75305

[52] Maldar, N. R., Ng, C. Y., Ean, L. W., Oguz, E., Fitriadhy, A., Kang, H. S., 2020. A Comparative Study on the Performance of a Horizontal Axis Ocean Current Turbine Considering Deflector and Operating Depths. *Sustainability*, 12(8), 3333. https://doi.org/10.3390/su12083333

[53] Kang, S., Borazjani, I., Colby, J. A., Sotiropoulos, F., 2012. Numerical Simulation of 3D Flow Past a Real-Life Marine Hydrokinetic Turbine. *Advances in Water Resources*, 39, 33-43. https://doi.org/10.1016/j.advwatres.2011.12.012